

See discussions, stats, and author profiles for this publication at: <https://www.researchgate.net/publication/351092147>

# Tungsten-containing high-entropy alloys: a focused review of manufacturing routes, phase selection, mechanical properties, and irradiation resistance properties

Article in Tungsten · April 2021

DOI: 10.1007/s42864-021-00081-x

CITATIONS

26

READS

507

9 authors, including:



Tianxin Li

Guizhou University

25 PUBLICATIONS 425 CITATIONS

SEE PROFILE



Enyu Guo

Dalian University of Technology

127 PUBLICATIONS 2,225 CITATIONS

SEE PROFILE



# Tungsten-containing high-entropy alloys: a focused review of manufacturing routes, phase selection, mechanical properties, and irradiation resistance properties

Tian-Xin Li<sup>1</sup> · Jun-Wei Miao<sup>1</sup> · En-Yu Guo<sup>1</sup> · He Huang<sup>2</sup> · Jun Wang<sup>3</sup> · Yi-Ping Lu<sup>1,4</sup> · Tong-Min Wang<sup>1</sup> · Zhi-Qiang Cao<sup>1</sup> · Ting-Ju Li<sup>1</sup>

Received: 1 January 2021 / Revised: 1 February 2021 / Accepted: 2 February 2021 / Published online: 23 April 2021  
© The Nonferrous Metals Society of China 2021

## Abstract

Alloying is one of the most effective means to confer superior properties to metal materials. For far too long, conventional W-based alloys were generally improved by the addition of minor elements. The exploitation of conventional W-based alloy is restricted to the corner of multielement phase diagrams with tiny compositional space. High-entropy alloys (HEAs) are a novel kind of alloys consisting of multi-principal alloying elements (usually more than 4) and have attracted increasing attention, since they were first reported in 2004. The emergence of HEAs filled the gap of the unexplored central region of multielement phase diagrams. Among them, tungsten-containing HEAs (TCHEAs) exhibit excellent mechanical properties, especially at extraordinarily elevated temperatures. Moreover, recent studies showed that TCHEAs had outstanding irradiation resistance properties. TCHEAs might serve as a promising candidate for plasma-facing materials in the fusion reactor. Many characteristics of TCHEAs are different from other HEAs due to the addition of tungsten with ultrahigh-melting temperature. Here, this paper aimed to introduce the manufacturing routes of TCHEAs; review the phase selection, mechanical properties, and irradiation resistance properties of TCHEAs; and propose the future prospects of TCHEAs.

**Keywords** Tungsten-containing high-entropy alloys · Irradiation resistance properties · Mechanical properties · Manufacturing routes · Phase selection

## 1 Introduction

In the last several decades, a lack of suitable plasma-facing materials (PFMs) has long been a grand challenge in the

field of fusion reactors. Conventional tungsten (W)-based alloys [1] are one of the serviceable candidates for PFMs due to their many advantages, such as high-melting point, low erosion, suppressed tritium retention, and reduced neutron activation [2]. However, the development of W-based alloys was stalled due to several disadvantages, such as irradiation-induced embrittlement, recrystallization-induced embrittlement, and high ductile-to-brittle transition temperature [3]. In such a context, extensive investigations of W-based binary alloys, such as W–Re [4], W–Ta [5, 6], W–V [6], W–Ti [6], W–Mo [7], and W–Cr [8], have been conducted. Although the exploitation of conventional W-based alloys tends to be extreme, the known binary alloys have their own drawbacks [2]. Therefore, it is urgent to develop novel tungsten-containing materials that can be used for PFMs.

Unlike conventional alloys consisting of one- or two-based elements, high-entropy alloys (HEAs) consist of multiple equimolar or nearly equimolar mixtures of elements (usually more than 4) [9, 10]. Figure 1 shows that the emergence of HEAs filled the gap of the unexplored

✉ En-Yu Guo  
eyguo@dlut.edu.cn

✉ Yi-Ping Lu  
luyiping@dlut.edu.cn

<sup>1</sup> Key Laboratory of Solidification Control and Digital Preparation Technology (Liaoning Province), School of Materials Science and Engineering, Dalian University of Technology, Dalian 116024, China

<sup>2</sup> Institute of Materials, China Academy of Engineering Physics, Mianyang 621907, China

<sup>3</sup> State Key Laboratory of Solidification Processing, Northwestern Polytechnical University, Xi'an 710072, China

<sup>4</sup> High Entropy Alloy Materials Engineering Research Center (Liaoning Province), School of Materials Science and Engineering, Dalian University of Technology, Dalian 116024, China

central region of multielement phase diagrams and dramatically expanded the compositional space of alloy design [11]. Since then, the focus of the material investigation has shifted from the corners of phase diagrams to a huge central region. A large number of studies indicated that HEAs had unusual mechanical, physical, and chemical properties due to several unique features, such as high entropy, sluggish diffusion, lattice distortion, and cocktail effects [12–16]. Among them, tungsten-containing HEAs (TCHEAs) combine the advantages of W-based refractory alloys and HEAs. A number of studies established that TCHEAs had excellent mechanical properties at elevated temperatures [17, 18] and irradiation resistance properties [3, 19]. For instance, representative WTaMoNbV TCHEA reported by Senkov et al. [18] had an amazing yield strength of 477 MPa at 1600 °C, which was far superior to that of a nickel-based superalloy. El-Atwani et al. [3] found that a novel WTaCrV TCHEA did not generate dislocation and exhibited outstanding irradiation resistance properties under Kr ion irradiation with 1 MeV at 800 °C. TCHEAs could be one of the promising candidates for PFMs due to these excellent characteristics [19]. However, few studies have classified TCHEAs into an individual category and discussed their characteristics individually. Indeed, the manufacturing routes and phase selection rules of TCHEAs were found to be slightly different from other HEAs on account of the addition of tungsten with ultrahigh-melting points.

In this paper, the research progress of TCHEAs as an individual category was explored. First, the manufacturing routes of TCHEAs were reviewed. Then, phase selection, mechanical properties, and irradiation resistance properties of TCHEAs were introduced and discussed in detail. Finally, the prospect and challenges of TCHEAs were proposed.

## 2 Manufacturing routes of TCHEAs

Various manufacturing routes to fabricate TCHEAs exist, which can be divided into three main subgroups using TCHEA morphology. Specifically, arc melting, spark plasma sintering (SPS), and additive manufacturing are the most common methods to fabricate bulk TCHEAs. Laser cladding deposition and magnetron sputtering are generally used to fabricate thin-film TCHEAs. Mechanical alloying (MA) is used to fabricate TCHEA powder. Manufacturing routes have a significant influence on the phase structure of TCHEAs. As shown in Table 1, the phase structure of TCHEAs fabricated by diverse routes may be different, even though the chemical components are the same. On one hand, different cooling rates lead to a liquid–solid nonequilibrium solidification process. On the other hand, different experimental conditions, such as sintering temperature, result in different completeness of element diffusion in a solid–solid diffusion process. Notable differences in phase structure were found in WTaMoNbV TCHEA fabricated by arc melting [18] and WTaMoNbV fabricated by MA and high-pressure/high-temperature technique [50]. The former using a rapid cooling rate was comprised of a single body-centered cubic (BCC) phase, while the latter contained two BCC phases.

In general, the manufacturing routes involving liquid–solid–solidification process with rapid cooling rates are favorable for obtaining TCHEAs with single-phase solid-solution structure compared with the manufacturing routes involving solid–solid diffusion process. First, liquid–solid–solidification process could suppress the chemical component heterogeneity due to the contribution to reaction of liquid phase. The all-solute atoms are mobile in a liquid phase and the chemical component of liquid phase is relatively homogeneous as a consequence. Second, relatively rapid cooling rates can suppress the formation of intermetallic compound. Consequently, additive manufacturing, laser cladding, and deposition magnetron sputtering being a representative subset of liquid–solid–solidification process with rapid cooling rates tend to prepare TCHEAs with single-phase solid-solution structure. The tendency to obtain TCHEAs with single-phase solid-solution structure of arc melting involving intermediate cooling rates is not significant compared with above-mentioned manufacturing routes with rapid cooling rates. The manufacturing routes belonging to solid–solid diffusion processes are difficult to prepare TCHEAs with homogeneous chemical component and microstructure because of the absence of liquid phase and imperfect diffusion reaction. In this section, various manufacturing routes of TCHEAs and the corresponding key process parameters have been discussed.

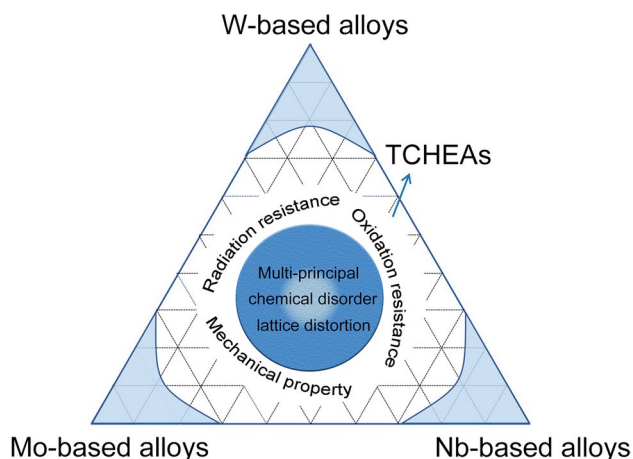


**Fig. 1** Respective occupied regions of conventional alloys and tungsten-containing high-entropy alloys on a ternary plot

**Table 1** Summary of chemical component, phase structure, and manufacturing routes of TCHEAs

Chemical component (atomic ratio)	Phase structure	Manufacturing route	References
CoCrFeNiW <sub>0.2</sub>	FCC + $\sigma$	Arc melting	[20]
CoCrFeNiW <sub>0.4</sub>	FCC + $\sigma$	Arc melting	[20]
CoCrFeNiW <sub>0.6</sub>	FCC + $\sigma$	Arc melting	[20]
CrFeNi <sub>2</sub> V <sub>0.5</sub> W <sub>0.25</sub>	FCC + $\sigma$	Arc melting	[21]
Nb <sub>18</sub> Ni <sub>18</sub> Ta <sub>18</sub> Ti <sub>18</sub> W <sub>18</sub> Al <sub>10</sub>	$\mu$ + BCC	Arc melting	[22]
NbNiTaTiW	$\mu$ + BCC	Arc melting	[22]
VCrFeTa <sub>0.3</sub> W <sub>0.3</sub>	BCC1 + BCC2	Arc melting	[23]
VCrFeTa <sub>0.4</sub> W <sub>0.4</sub>	BCC + Laves	Arc melting	[23]
VCrFeTaW	BCC1 + BCC2 + Laves	Arc melting	[23]
Co <sub>2</sub> Mo <sub>0.5</sub> Ni <sub>2</sub> VW <sub>0.5</sub>	FCC + BCC + $\mu$	Arc melting	[24]
Co <sub>2</sub> Mo <sub>0.6</sub> Ni <sub>2</sub> VW <sub>0.6</sub>	FCC + BCC + $\mu$	Arc melting	[24]
Co <sub>2</sub> Mo <sub>0.8</sub> Ni <sub>2</sub> VW <sub>0.8</sub>	FCC + BCC + $\mu$	Arc melting	[24]
Co <sub>2</sub> MoNi <sub>2</sub> VW	FCC + BCC + $\mu$	Arc melting	[24]
Co <sub>2</sub> Mo <sub>1.5</sub> Ni <sub>2</sub> VW <sub>1.5</sub>	FCC + BCC + $\mu$	Arc melting	[24]
Co <sub>2</sub> Mo <sub>1.75</sub> Ni <sub>2</sub> VW <sub>1.75</sub>	FCC + BCC + $\mu$	Arc melting	[24]
CrFeNiV <sub>0.5</sub> W <sub>0.25</sub>	FCC + BCC + $\sigma$	Arc melting	[25]
CrFeNiV <sub>0.5</sub> W <sub>0.5</sub>	FCC + BCC + $\sigma$	Arc melting	[25]
CrFeNiV <sub>0.5</sub> W <sub>0.75</sub>	FCC + BCC + $\sigma$	Arc melting	[25]
CrFeNiV <sub>0.5</sub> W	FCC + BCC + $\sigma$	Arc melting	[25]
CrFeNi <sub>2</sub> V <sub>0.5</sub> W <sub>0.25</sub>	FCC + BCC + $\sigma$	Arc melting	[25]
CrFeNi <sub>2</sub> V <sub>0.5</sub> W <sub>0.5</sub>	FCC + BCC + $\sigma$	Arc melting	[25]
CrFeNi <sub>2</sub> V <sub>0.5</sub> W <sub>0.75</sub>	FCC + BCC + $\sigma$	Arc melting	[25]
CrFeNi <sub>2</sub> V <sub>0.5</sub> W	FCC + BCC + $\sigma$	Arc melting	[25]
HfNbTaTiZrW	BCC1 + BCC2	Arc melting	[26]
HfNbTaTiZrMoW	BCC1 + BCC2	Arc melting	[26]
Cr <sub>2</sub> MoNbTaVW	BCC1 + BCC2	Arc melting	[27]
CrMoNbTiW	BCC	Arc melting	[28]
VCrFeTa <sub>0.1</sub> W <sub>0.1</sub>	BCC	Arc melting	[23]
VCrFeTa <sub>0.2</sub> W <sub>0.2</sub>	BCC	Arc melting	[23]
ReMoTaW	BCC	Arc melting	[29]
NbMoTaW	BCC	Arc melting	[18]
Re <sub>0.5</sub> NbMoTaW	BCC	Arc melting	[30]
ReNbMoTaW	BCC	Arc melting	[30]
VNbTaMoW	BCC	Arc melting	[18]
ReTaWNbMo	BCC	Arc melting	[31]
Mo <sub>5</sub> Nb <sub>10</sub> Ta <sub>35</sub> V <sub>15</sub> W <sub>35</sub>	BCC	Arc melting	[32]
Mo <sub>5</sub> Nb <sub>25</sub> Ta <sub>30</sub> V <sub>5</sub> W <sub>35</sub>	BCC	Arc melting	[32]
Mo <sub>5</sub> Nb <sub>30</sub> Ta <sub>35</sub> V <sub>15</sub> W <sub>15</sub>	BCC	Arc melting	[32]
Mo <sub>5</sub> Nb <sub>35</sub> Ta <sub>15</sub> V <sub>10</sub> W <sub>35</sub>	BCC	Arc melting	[32]
Mo <sub>10</sub> Nb <sub>35</sub> Ta <sub>25</sub> V <sub>5</sub> W <sub>25</sub>	BCC	Arc melting	[32]
Mo <sub>15</sub> Nb <sub>35</sub> Ta <sub>35</sub> V <sub>5</sub> W <sub>10</sub>	BCC	Arc melting	[32]
CrMoReVW	BCC	Arc melting	[32]
Cr <sub>5</sub> Mo <sub>5</sub> Re <sub>20</sub> V <sub>35</sub> W <sub>35</sub>	BCC	Arc melting	[32]
CrMoVW	BCC	Arc melting	[33]
Ti <sub>0.25</sub> NbMoTaW	BCC	Arc melting	[34]
Ti <sub>0.5</sub> NbMoTaW	BCC	Arc melting	[34]
Ti <sub>0.75</sub> NbMoTaW	BCC	Arc melting	[34]
TiNbMoTaW	BCC	Arc melting	[34]
NbTaVW	BCC	Arc melting	[35]
NbTaTiVW	BCC	Arc melting	[36]
Cr <sub>0.5</sub> MoNbTaVW	BCC	Arc melting	[27]

**Table 1** (continued)

Chemical component (atomic ratio)	Phase structure	Manufacturing route	References
CrMoNbTaVW	BCC	Arc melting	[27]
CrMoNbTiW	BCC	Arc melting	[28]
MoNbTaW	BCC	Additive manufacturing	[37]
MoFeCrTiWAlNb	BCC + IM + Laves	Laser cladding deposition	[38]
W <sub>0.16</sub> NbMoTa	BCC	Laser cladding deposition	[39]
W <sub>0.33</sub> NbMoTa	BCC	Laser cladding deposition	[39]
W <sub>0.53</sub> NbMoTa	BCC	Laser cladding deposition	[39]
TiZrNbWMo	BCC + $\beta$	Laser cladding deposition	[40]
WMoNbZrV	BCC	Mechanical alloying	[41]
FeCoNiAlMnW	FCC	Magnetron sputtering	[42]
CuMoTaWV	BCC	Magnetron sputtering	[43]
W <sub>23.75</sub> Mo <sub>23.75</sub> Nb <sub>23.75</sub> Ti <sub>23.75</sub> Cr <sub>5</sub>	BCC + Laves	Spark plasma sintering	[44]
W <sub>22.5</sub> Mo <sub>22.5</sub> Nb <sub>22.5</sub> Ti <sub>22.5</sub> Cr <sub>10</sub>	BCC + Laves	Spark plasma sintering	[44]
W <sub>21.25</sub> Mo <sub>21.25</sub> Nb <sub>21.25</sub> Ti <sub>21.25</sub> Cr <sub>15</sub>	BCC + Laves	Spark plasma sintering	[44]
WMoNbTiCr	BCC + Laves	Spark plasma sintering	[44]
AlCuTaVW	FCC1 + FCC2 + B2	Spark plasma sintering	[45]
WTaMoNbVCrZrTi	BCC + FCC + IM	Spark plasma sintering	[46]
NbMoTaWVCr	BCC + Laves + Ta <sub>2</sub> VO <sub>6</sub>	Spark plasma sintering	[47]
CuMoTaWV	BCC + IM	Spark plasma sintering	[48]
W <sub>0.3</sub> (TaTiCrV) <sub>0.7</sub>	BCC + IM + Laves	Spark plasma sintering	[2]
W <sub>0.4</sub> (TaTiCrV) <sub>0.6</sub>	BCC + IM + Laves	Spark plasma sintering	[2]
W <sub>0.5</sub> (TaTiCrV) <sub>0.5</sub>	BCC + IM + Laves	Spark plasma sintering	[2]
W <sub>0.6</sub> (TaTiCrV) <sub>0.4</sub>	BCC + IM + Laves	Spark plasma sintering	[2]
W <sub>0.7</sub> (TaTiCrV) <sub>0.3</sub>	BCC + IM + Laves	Spark plasma sintering	[2]
W <sub>0.8</sub> (TaTiCrV) <sub>0.2</sub>	BCC + IM + Laves	Spark plasma sintering	[2]
W <sub>0.9</sub> (TaTiCrV) <sub>0.1</sub>	BCC + IM + Laves	Spark plasma sintering	[2]
CoCrFeNiMnW <sub>0.25</sub>	FCC	Spark plasma sintering	[49]

BCC, body-centered cubic phase; FCC, face-centered cubic phase; IM, intermetallic compound phase;  $\sigma$ , FeV-type phase;  $\beta$ , Ti–W binary solid-solution phase;  $\mu$ , Co<sub>7</sub>Mo<sub>6</sub>-type phase; Laves, Laves phase; FCC1(BCC1) and FCC2(BCC2), two two different types of FCC(BCC) phases; B2, B2-type ordering phase

## 2.1 Arc melting

Arc melting is the main manufacturing route to fabricate TCHEAs. The local temperature ( $> 6000$  °C) generated by arc discharge greatly exceeds the melting point ( $T_m$ ) of W (3406 °C). Refractory elements, such as W, Ta, Mo, and Nb, can be melted rapidly in the arc melting process. However, considerable challenges still exist in obtaining the homogeneous casting ingots. First, significant differences in respective  $T_m$  of multiple elements in TCHEAs can cause destructive volatilization. Second, the inferior casting castability induced by W with high fluid viscosity makes it difficult to ensure the homogeneity of casting ingots.

For the former specific issue, Cr is a common alloying addition in TCHEAs to improve the oxidation and corrosion resistance properties [51]. However, Cr volatilizes easily in a melting process due to its high-saturated vapor pressure [33]. In fact, the boiling point of Cr is 2671 °C, which is less than that of W by  $\sim 800$  °C. In an actual melting process, the component elements with  $T_m$  of more than 2671 °C do

not still melt entirely before Cr initiate to volatilize. An artful method was proposed by Ikeuchi et al. [33] to fabricate CrMoVW TCHEAs without severe evaporation of Cr. The melting process of CrMoVW TCHEAs is separated into two steps based on the respective melting point of component elements. The pure raw materials of Mo, V, and W with high  $T_m$  are melted first, so that  $T_m$  of the Mo–V–W mixture decreases to 2645 °C, which is slightly lower than the boiling point of Cr [33]. Then, Cr is added to the Mo–V–W mixture obtained from the previous step. Therefore, the evaporation process is suppressed by accurately adjusting and controlling the melting process of TCHEAs [33]. Besides, the differences in  $T_m$  also cause microsegregation in TCHEAs [52]. Elements with high  $T_m$  solidify first and lead to a high concentration in the dendritic regions. Conversely, the rest of the elements with low  $T_m$  prefer to exist in interdendritic regions.

Inferior casting castability issues also plague the development of TCHEAs. Eutectic alloys with good casting fluidity are widely used in many fields [53]. Recently, eutectic HEAs



(EHEAs) were proposed to overcome inferior castability and remove obstacles for the technological applications of HEAs [54]. Based on this idea, eutectic TCHEAs were designed by Jiang et al. [24, 25]. The inferior castability of TCHEAs was effectively improved by the eutectic alloying design.

## 2.2 MA processing

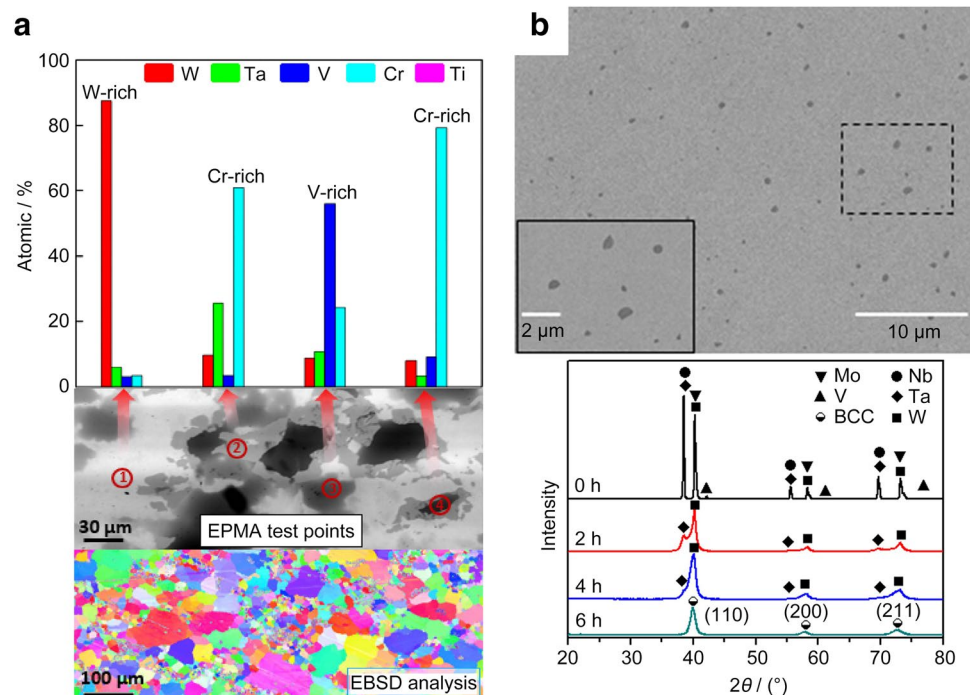
MA is an effective way to obtain TCHEA powder. In general, MA is preferred to form supersaturated solid solutions [55], as it is more suitable for fabricating a single and solid-solution phase TCHEA. Nevertheless, impurities may be introduced by the ball medium or oxygen in the air so that an appropriate MA process is adopted. Kang et al. [56] applied a high-energy ball-milling process using tungsten carbide balls for 6 h at  $300 \text{ r} \cdot \text{min}^{-1}$  to fabricate a single and BCC solid-solution phase WNbMoTaV TCHEA. All procedures were carried out inside a glove box, and therefore, few oxides were observed in X-ray diffraction (XRD) patterns and scanning electron microscope (SEM) micrographs. Long et al. [47] conducted a similar process to fabricate WNbMoTaVCr with stainless-steel balls. The results showed that it required at least 40-h balling time to form a single and BCC solid solution. Furthermore,  $\text{Ta}_2\text{VO}_6$  oxide particles were observed in the BCC matrix due to the absence of using a glove box [47]. Tong et al. [57] investigated the effect of different process control agents on the MA process of TCHEAs. The results showed that it had little effect on the phase structure of TCHEAs with or without a control agent in an MA process, but the small-size powder could

be obtained without a control agent. In a word, the ball mill medium, the balling time, and the antioxidation measure are the critical factors that should be considered in particular for an MA process.

## 2.3 Powder metallurgy

Powder metallurgy, including SPS, is an important route to fabricate the bulk TCHEAs. In fact, conventional bulk W-based alloys are almostly fabricated by powder metallurgy methods. The sintering temperature of W-based alloys is usually set over  $2200^\circ\text{C}$  in a hot-pressed sintering process [58]. In an SPS process, the sintering temperature reduces to  $1800^\circ\text{C}$  [55]. A homogeneous microstructure is difficult to obtain if the sintering temperature does not reach the threshold of fast-diffusion temperature. A prior MA process is critical in a sintering process when the sintering temperature is lower than the threshold temperature [47]. For instance, as shown in Fig. 2a, WTaVCr TCHEAs [59] are fabricated by directly sintering at  $1500^\circ\text{C}$  without a prior MA process, and severe microsegregation is observed. On the contrary, WTaMoNbV TCHEA is fabricated by SPS at  $1500^\circ\text{C}$  with a prior MA process, which consists of a homogeneous solid-solution phase, indicating that the microsegregation is significantly reduced, as shown in Fig. 2b [56]. Recently, Han et al. [60] conducted a novel method to fabricate WTaMoNb TCHEA powders by pressureless sintering and MA. First, a pressureless SPS process was conducted at  $1900^\circ\text{C}$  to obtain porous samples. Then, the porous samples were smashed by ball milling to prepare TCHEA powders with homogeneous

**Fig. 2** **a** Chemical compositions and microstructure of WTaCrV TCHEAs fabricated by SPS sintered at  $1500^\circ\text{C}$  without prior MA process. Reproduced with permission from Ref. [59] Copyright 2018 Elsevier. **b** SEM micrographs of WTaMoNbV TCHEAs fabricated by SPS sintered at  $1500^\circ\text{C}$  with prior MA process and XRD patterns of the 2-, 4-, and 6-h ball-milled WTaMoNbV TCHEAs powders. Reproduced with permission from Ref. [56] Copyright 2018 Elsevier



chemical composition. This original method to fabricate TCHEA powders did not adopt a long-term high-energy MA process and reduced the impurities to a great extent.

## 2.4 Other processing methods

Other processing methods, such as laser cladding, magnetron sputtering, and additive manufacturing, are also used to fabricate TCHEAs. The cooling rate in the laser cladding is high leading to fine-grained microstructures [38, 39, 61]. Moreover, it generates supersaturated and metastable solid-solution phase of TCHEAs by a rapid cooling process, because it does not have enough time for nucleation and growth of intermetallic compounds. That is, the formation of an intermetallic compound is inhibited. MoFe<sub>1.5</sub>CrTiWAlNb<sub>x</sub> ( $x=1.5, 2, 2.5$ , and 3) TCHEA coating consisting of BCC and C14-type Laves phases was fabricated by Wang et al. [61]. The microhardness of MoFe<sub>1.5</sub>CrTiWAlNb<sub>3</sub> showed a maximum of 910 HV, which was approximately three times that of the steel matrix.

Magnetron sputtering technique is a kind of physical vapor deposition usually used to fabricate nanocrystalline thin-film TCHEAs [42, 43, 62–64]. High-entropy effects have been found to improve the stability of nanocrystalline TCHEAs [62]. In the nanopillar compression test, nanocrystalline TCHEAs exhibit extraordinarily high yield strengths up to 10 GPa [62].

Additive manufacturing is beneficial to fabricate TCHEAs with complex hierarchical structures [37, 49, 65]. Melia et al. [65] indicated that additive manufacturing could fabricate TCHEAs with a fine homogeneous cellular microstructure. The high-throughput additive manufacturing will hopefully help explore novel TCHEAs with excellent performance [65].

## 3 Phase selection in TCHEAs

Simple solid-solution (SSS) structure has been found to bring many advantages for HEAs in terms of mechanical properties, irradiation resistance properties, and oxidation resistance properties [11, 66–68]. Thus, the criteria of phase selection have become one of the hottest issues in the study of HEAs [69]. The empirical parametric models [69–73], calculation of phase diagram (CALPHAD) [74], first-principle calculation [75], and machine learning [76] were used to explore the phase selection in HEAs. As a particular part of HEAs, the criteria of phase selection in TCHEAs are slightly different from others due to the more severe lattice distortion and high  $T_m$ . These two intrinsic features have a vital influence on the stability of an SSS structure. As shown in Fig. 3, the difference in the atomic radius ( $\delta$ ) is a common parameter to reflect the lattice

distortion in the  $\Lambda$  [77, 78] $\delta$ , and  $\gamma$  models [72]. However, recent evidence suggested that more severe lattice distortion occurred in BCC HEAs, including most TCHEAs, which was an order of magnitude higher than that of FCC HEAs with similar  $\delta$  value [79–81]. In fact,  $\delta$  cannot accurately quantify the lattice distortion in TCHEAs.

In addition,  $T_m$  calculated by rule-of-mixtures is a critical parameter in many empirical parametric models, such as the  $\Omega$  [82],  $H_f$  [73], and  $\Phi$  models [83]. TCHEAs with high  $T_m$  crystallize earlier in a solidification process, and it is regarded to reduce mixing Gibbs free energy according to Gibbs relationship (Eq. (1)):

$$\Delta G_{\text{mix}} = \Delta H_{\text{mix}} - T_m \Delta S_{\text{mix}} \quad (1)$$

where  $\Delta G_{\text{mix}}$  is the mixing Gibbs free energy,  $\Delta H_{\text{mix}}$  is the mixing enthalpy, and  $\Delta S_{\text{mix}}$  is the mixing entropy. Obviously,

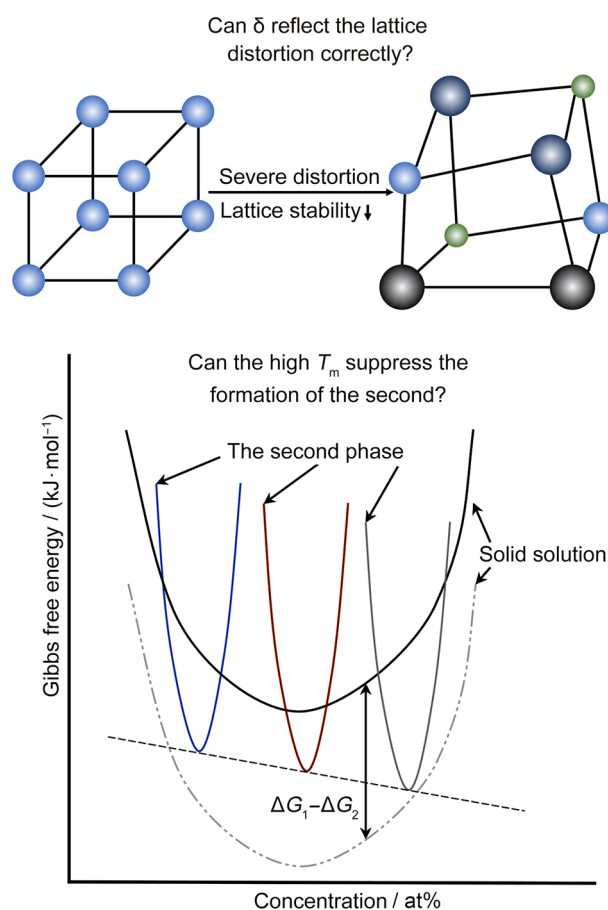


**Fig. 3** Schematic diagram of the effect of parameters  $\delta$  and  $T_m$  on the stability of a phase structure. Severe lattice distortion in TCHEAs reduces the stability of SSS, and high  $T_m$  can reduce the Gibbs free energy of SSS in TCHEAs. Two questions as below need to be discussed. Can  $\delta$  reflect the lattice distortion correctly? Can the high  $T_m$  suppress the formation of the second? Note:  $\Delta G_1$  and  $\Delta G_2$  are the Gibbs free energy of the solid solution with low  $T_m$  and high  $T_m$

high  $T_m$  could reinforce the high-entropy effect by a term of  $T_m \Delta S_{\text{mix}}$ . The following two problems appear during the phase selection of TCHEAs: can the  $\delta$  parameter-related model be applied for TCHEAs? Would high  $T_m$  promote the formation of SSS? Reappraising the accuracy of empirical parametric models using  $\delta$  and  $T_m$  and verifying whether a misestimate exists are significant.

In this study, some representative empirical parametric models were selected and divided into two categories:  $\delta$ -related models and  $T_m$ -related models. Then, their applicability in TCHEAs was verified. The criteria and expression for each model are shown in Table 2.

### 3.1 Atomic size-related models

Only as-cast samples were selected for study to rule out the effects of manufacturing routes on phase selection. The correlative calculated results are listed in Table 3.

$\delta$ -related models are generally derived from the Hume–Rothery rules, indicating that the condition of  $\delta < 15\%$  is propitious to form binary solid solutions [84]. The excessive  $\delta$  is unfavorable for the formation of SSS. Specifically, Singh et al. [77] proposed the  $\Lambda$  model involving  $\Delta S_{\text{mix}}$  and  $\delta$ . SSS would form if the  $\Lambda$  value was greater than 0.96. Figure 4a shows that the  $\Lambda$  model was relatively accurate for TCHEAs. A majority of SSS and IMC were divided clearly by the boundary of  $\Lambda = 0.96$ . The overall accuracy (the overall accuracy was equal to the number of coincident cases over the number of total cases) was 83.3%, suggesting that the  $\Lambda$ -model could determine phase selection in TCHEAs well.

However, the effect of the model involving  $\Delta H_{\text{mix}}$  and  $\delta$  on phase selection in TCHEAs was not effective. The

$\delta$  model proposed by Guo et al. [78] demonstrated that it tended to form SSS if  $\Delta H_{\text{mix}}$  of HEAs was close to 0; meanwhile,  $\delta$  was not too large. As shown in Fig. 4b, most TCHEAs fell into the SSS region regardless of whether they were SSS or IMC. The overall accuracy of the  $\delta$  model was only 55.4%, meaning that the  $\delta$  model hardly applied to the TCHEA system. The effect of  $\Delta H_{\text{mix}}$  on distinguishing SSS and IMC was nearly negligible. Although the condition of  $\delta < 6.6\%$  could not distinguish the SSS region obviously, most TCHEAs were assembled under the condition of  $< \delta$  3%. Indeed, severe lattice distortion existed in TCHEAs to hinder the formation of SSS, although  $\delta$  merely reached 3%. Song et al. [79] proposed ab initio calculation for refractory HEAs with the BCC structure including most TCHEAs and revealed more severe lattice distortion in BCC HEAs due to less close-packed structure than that of the FCC HEAs. Moreover, local chemical environments [85] and the special phenomenon of charge transfer in BCC HEAs are important in lattice distortion [84]. Although the parameter  $\delta$  was not enough to accurately describe the local lattice distortion [79], the condition of  $\delta < 3.0\%$  was proposed in this study to distinguish the SSS region effectively for TCHEAs.

Wang et al. [72] proposed the  $\gamma$  model involving the ratio between the solid angles of the smallest and largest atoms, which could affect the stability of a lattice, leading to the formation of SSS. Compared with the  $\delta$  model, the  $\gamma$  model was especially suitable for the system containing minor elements, because the parameter  $\gamma$  correlated with the chemical element types rather than the chemical element content. As shown in Fig. 4c, the  $\gamma$  model with the boundary conditions of  $\gamma < 1.175$  and  $-11.6 < \Delta H_{\text{mix}} < 3.2 \text{ kJ} \cdot \text{mol}^{-1}$  could not distinguish the SSS region as well. The overall accuracy of the  $\delta$  model was only 58.9%. Interestingly, the condition of  $\gamma < 1.110$  could distinguish

**Table 2** Summary of  $\delta$ - and  $T_m$ -related models

Category	Model	Expression	Criterion	References
$\delta$ -Related models	$\Lambda$	$\Lambda = \frac{\Delta S_{\text{mix}}}{\delta^2}$	$\Lambda > 0.96$	[77]
	$\delta$	$\delta = \sqrt{\sum_{i=1}^n c_i \left(1 - \frac{r_i}{\bar{r}}\right)^2}$	$-11.6 < \Delta H_{\text{mix}} < 3.2 \text{ kJ/mol}$ $\delta < 6.6\%$	[78]
	$\gamma$	$\gamma = \frac{1 - \sqrt{(r_s + \bar{r})^2 - \bar{r}^2} / (r_l + \bar{r})^2}{1 - \sqrt{(r_l + \bar{r})^2 - \bar{r}^2} / (r_l + \bar{r})^2}$	$-11.6 < \Delta H_{\text{mix}} < 3.2 \text{ kJ/mol}$ $\gamma < 1.175$	[72]
$T_m$ -related models	$\Omega$	$\Omega = \frac{T_m \Delta S_{\text{mix}}}{\Delta H_{\text{mix}}}$	$\Omega \geq 1.1$	[82]
	$\Delta H_f$	$\Delta H_f = \min(\Delta H_f^{ij}),$ $i, j = 1, 2, 3 \dots n, i \neq j$	$-T_c \Delta S_{\text{mix}} < \Delta H_f < 3.57 \text{ meV/atom}$	[73]
	$\Phi$	$\Phi = \frac{\Delta G_{\text{ss}}}{- \Delta G_{\text{mix}} }$	$\Phi \geq 1$	[83]

$\Delta S_{\text{mix}}$ , The configuration entropy of a random solid solution;  $\Delta H_{\text{mix}}$ , the enthalpy of mixing for a random solid solution;  $r_s$ , the smallest atomic radius;  $r_l$ , the largest atomic radius;  $\bar{r}$ , the average atomic radius;  $\Delta H_f^{ij}$ , the lowest formation enthalpies of binary element pairs between  $i$ th and  $j$ th;  $T_c$ , annealing temperature for annealed alloys or critical temperature (equal to  $0.55 T_m$ ) for as-cast alloys;  $\Delta G_{\text{ss}}$ , the formation energy of random solid solution; the lowest (intermetallic) or highest (segregated) Gibbs free energy calculated from each possible binary pairs

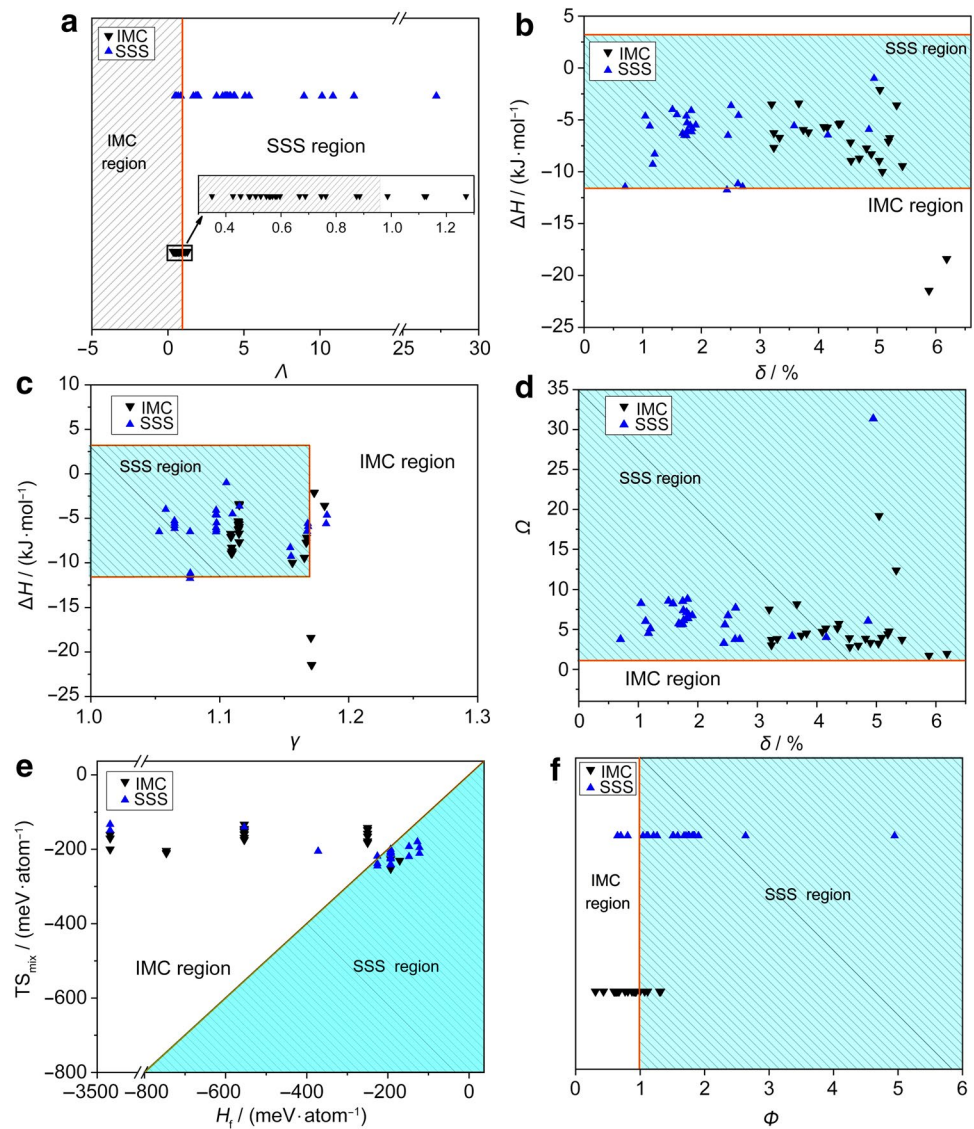


**Table 3** Alloys selected and correlative calculated results for TCHEAs

Chemical component (atomic ratio)	References	Phase type	$\Lambda$	$\delta$	$\gamma$	$\Omega$	$\Delta H_f$	$\Phi$
CoCrFeNiW <sub>0.4</sub>	[20]	IMC	S	S	S	S	I	S
CoCrFeNiW <sub>0.6</sub>	[20]	IMC	S	S	S	S	I	S
CrFeNi <sub>2</sub> V <sub>0.5</sub> W <sub>0.25</sub>	[21]	IMC	S	S	S	S	I	I
Nb <sub>18</sub> Ni <sub>18</sub> Ta <sub>18</sub> Ti <sub>18</sub> W <sub>18</sub> Al <sub>10</sub>	[22]	IMC	I	I	I	S	I	I
NbNiTaTiW	[22]	IMC	I	S	S	S	I	I
VCrFeTa <sub>0.3</sub> W <sub>0.3</sub>	[23]	IMC	I	S	S	S	I	I
VCrFeTa <sub>0.4</sub> W <sub>0.4</sub>	[23]	IMC	I	S	S	S	I	I
VCrFeTaW	[23]	IMC	I	S	S	S	I	I
Co <sub>2</sub> Mo <sub>0.5</sub> Ni <sub>2</sub> VW <sub>0.5</sub>	[24]	IMC	I	S	S	S	I	I
Co <sub>2</sub> Mo <sub>0.6</sub> Ni <sub>2</sub> VW <sub>0.6</sub>	[24]	IMC	I	S	S	S	I	I
Co <sub>2</sub> Mo <sub>0.8</sub> Ni <sub>2</sub> VW <sub>0.8</sub>	[24]	IMC	I	S	S	S	I	I
Co <sub>2</sub> MoNi <sub>2</sub> VW	[24]	IMC	I	S	S	S	I	I
Co <sub>2</sub> Mo <sub>1.5</sub> Ni <sub>2</sub> VW <sub>1.5</sub>	[24]	IMC	I	S	S	S	I	I
Co <sub>2</sub> Mo <sub>1.75</sub> Ni <sub>2</sub> VW <sub>1.75</sub>	[24]	IMC	I	S	S	S	I	I
CrFeNiV <sub>0.5</sub> W <sub>0.25</sub>	[25]	IMC	S	S	S	S	I	I
CrFeNiV <sub>0.5</sub> W <sub>0.5</sub>	[25]	IMC	I	S	S	S	I	I
CrFeNiV <sub>0.5</sub> W <sub>0.75</sub>	[25]	IMC	I	S	S	S	I	I
CrFeNiV <sub>0.5</sub> W	[25]	IMC	I	S	S	S	I	I
CrFeNi <sub>2</sub> V <sub>0.5</sub> W <sub>0.25</sub>	[25]	IMC	S	S	S	S	I	I
CrFeNi <sub>2</sub> V <sub>0.5</sub> W <sub>0.5</sub>	[25]	IMC	I	S	S	S	I	I
CrFeNi <sub>2</sub> V <sub>0.5</sub> W <sub>0.75</sub>	[25]	IMC	I	S	S	S	I	I
CrFeNi <sub>2</sub> V <sub>0.5</sub> W	[25]	IMC	I	S	S	S	I	I
HfNbTaTiZrW	[26]	IMC	I	S	I	S	S	I
HfNbTaTiZrMoW	[26]	IMC	I	S	S	S	S	S
Cr <sub>2</sub> MoNbTaVW	[27]	IMC	I	S	S	S	S	S
CoCrFeNiW <sub>0.2</sub>	[28]	SSS	S	S	S	S	I	S
CrMoNbTiW	[23]	SSS	I	S	S	S	I	S
VCrFeTa <sub>0.1</sub> W <sub>0.1</sub>	[23]	SSS	I	S	S	S	I	S
VCrFeTa <sub>0.2</sub> W <sub>0.2</sub>	[29]	SSS	I	S	S	S	I	S
ReMoTaW	[18]	SSS	S	S	S	S	I	I
NbMoTaW	[30]	SSS	S	S	S	S	S	S
Re <sub>0.5</sub> NbMoTaW	[30]	SSS	S	S	S	S	S	I
ReNbMoTaW	[18]	SSS	S	S	S	S	S	I
VNbTaMoW	[31]	SSS	S	S	S	S	S	S
ReTaWNbMo	[32]	SSS	S	S	S	S	S	S
Mo <sub>5</sub> Nb <sub>10</sub> Ta <sub>35</sub> V <sub>15</sub> W <sub>35</sub>	[32]	SSS	S	S	S	S	S	S
Mo <sub>5</sub> Nb <sub>25</sub> Ta <sub>30</sub> V <sub>5</sub> W <sub>35</sub>	[32]	SSS	S	S	S	S	S	S
Mo <sub>5</sub> Nb <sub>30</sub> Ta <sub>35</sub> V <sub>15</sub> W <sub>15</sub>	[32]	SSS	S	S	S	S	S	S
Mo <sub>5</sub> Nb <sub>35</sub> Ta <sub>15</sub> V <sub>10</sub> W <sub>35</sub>	[32]	SSS	S	S	S	S	S	S
Mo <sub>10</sub> Nb <sub>35</sub> Ta <sub>25</sub> V <sub>5</sub> W <sub>25</sub>	[32]	SSS	S	S	S	S	S	S
Mo <sub>15</sub> Nb <sub>35</sub> Ta <sub>35</sub> V <sub>5</sub> W <sub>10</sub>	[32]	SSS	S	S	S	S	S	S
CrMoReVW	[32]	SSS	S	S	I	S	S	S
Cr <sub>5</sub> Mo <sub>5</sub> Re <sub>20</sub> V <sub>35</sub> W <sub>35</sub>	[33]	SSS	S	S	I	S	S	S
CrMoVW	[34]	SSS	I	S	S	S	S	S
Ti <sub>0.25</sub> NbMoTaW	[34]	SSS	S	S	S	S	S	S
Ti <sub>0.5</sub> NbMoTaW	[34]	SSS	S	S	S	S	S	S
Ti <sub>0.75</sub> NbMoTaW	[34]	SSS	S	S	S	S	S	S
TiNbMoTaW	[35]	SSS	S	S	S	S	S	S
NbTaVW	[36]	SSS	S	S	S	S	S	S
NbTaTiVW	[27]	SSS	S	S	S	S	S	S
Cr <sub>0.5</sub> MoNbTaVW	[27]	SSS	S	S	S	S	S	S
CrMoNbTaVW	[28]	SSS	S	S	S	S	S	S

SSS or S, simple solid-solution phase; IMC or I, intermetallic compounds containing phase or solid-solution multiphase

**Fig. 4** Empirical parametric models used to delineate the phase selection in TCHEAs. **a**  $\Lambda$  model; **b**  $\delta$  model; **c**  $\gamma$  model; **d**  $\Omega$  model; **e**  $\Delta H_f$  model; **f**  $\Phi$  model.



the SSS region much better than the former condition. It is suggested that there is more severe lattice distortion existing in TCHEAs, which is similar to the  $\delta$  model. In all, the  $\Lambda$  model, depending on the relationship between  $\Delta S_{mix}$  and  $\delta$ , was more accurate than the  $\delta$  and  $\gamma$  models, depending on the values of the parameters  $\Delta H_{mix}$  and  $\delta$ . A possible explanation for this might be that severe lattice distortion existing in TCHEAs reduces the stability of crystal lattice. The less tolerance of lattice distortion could exist in TCHEAs compared with other HEAs. Furthermore, the effect of  $\Delta S_{mix}$  was dominant for TCHEAs compared with  $\Delta H_{mix}$  for TCHEAs.

### 3.2 Temperature-related models

The second category of the empirical parametric models is the temperature-related models. Yang et al. [82] proposed the  $\Omega$  model, who suggested that SSS would form if the term  $T_m \Delta S_{mix}$  was dominant instead of the term  $\Delta H_{mix}$ . As shown in Fig. 4d, the  $\Omega$  model almost completely failed to distinguish the IMC region. The overall accuracy of the  $\Omega$  model was only 55.4%. First, the  $\Omega$  model only considered mixing Gibbs free energy of solid solution itself, and did not consider the relationship between the formation energy of intermetallic compound and solid solution. Second, the rule-of-mixtures  $T_m$  of TCHEAs increased seriously by the addition of W, while the effects of  $T_m$  were overestimated.

An  $\Delta H_f$  model was proposed by Troparevsky et al. [73].  $\Delta H_f$  was defined as the lowest formation enthalpy of

intermetallic compound of each possible binary element pairs, which was calculated by the density functional theory. SSS would achieve a dominant position rather than intermetallic compound if  $\Delta H_f$  was greater than the mixing energy, expressed as  $-T_c \Delta S_{\text{mix}}$ , where  $T_c$  is the critical temperature. For the  $\Delta H_f$  model,  $T_c$  (equal to  $0.55 T_m$  for as-cast alloys) was selected instead of  $T_m$ , because  $T_c$  represented the threshold temperature for the atom fast-diffusion process. Phase decomposition is not easy to occur if temperature condition is lower than  $T_c$ . The maximum value of  $\Delta H_f$  of SSS alloys obtained by statistical analysis was assumed to be 3.57 meV/atom, and it was set as the upper limit of the  $\Delta H_f$  model [73]. As shown in Fig. 4e, the accuracy of the  $\Delta H_f$  model significantly improved compared with the  $\Omega$  model, especially for the IMC region. The overall accuracy of the  $\Omega$  model increased to 85.2%. King et al. [83] modified the  $\Delta H_f$  model and proposed the  $\Phi$  model, which introduced chemical, elastic, and structural contributions to the formation enthalpy. As shown in Fig. 4f, the  $\Phi$  model significantly distinguished the SSS and IMC regions, with 87.5% overall accuracy.

All in all, the  $\Omega$  model was not applicable to TCHEAs, because it did not consider the relationship between the formation energy of the intermetallic compound and solid solution. On the contrary, the  $\Delta H_f$  and  $\Phi$  models had clear physical significance and more acceptable accuracy for TCHEAs. The relationship between the solid solution and intermetallic compound was critical for phase selection in TCHEAs.

## 4 Properties of TCHEAs

### 4.1 Mechanical properties

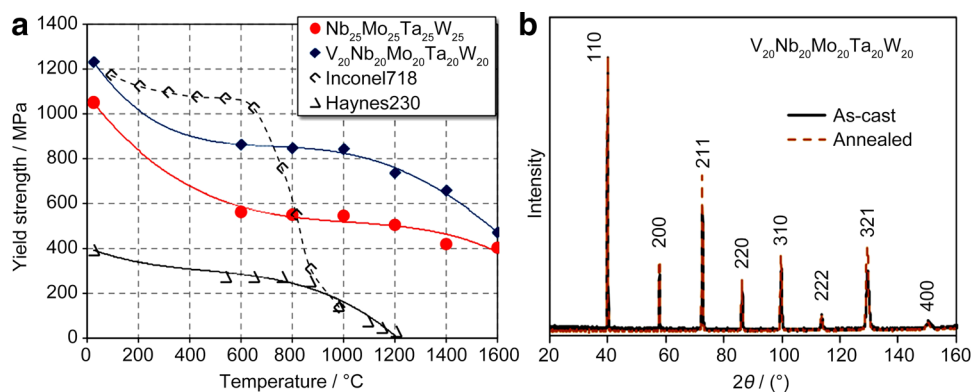
The first two representative TCHEAs, WNbMoTa, and WNbMoTaV, were proposed by Senkov et al. [18]. in 2010. These two TCHEAs were prepared by vacuum arc melting and indexed as a BCC single phase by XRD patterns. WNbMoTa and WNbMoTaV possessed excellent mechanical

properties at high temperatures [17]. As shown in Fig. 5, the yield stress of WNbMoTaV reached 477 MPa at 1600 °C. The yield stress of TCHEAs was considerably higher than that of superalloys, such as Inconel 718 and Haynes 230, whose yield stress was less than 250 MPa at 1000 °C. Moreover, the disordered BCC structure of TCHEAs still remained stable even after annealing at 1400 °C for 19 h [17].

On the basis of the aforementioned results, Zou et al. [63] reported that WNbMoTa TCHEA had a stable phase structure at 1800 °C for 17 days. The micropillar of WNbMoTa TCHEA had two-to-five times higher strength than pure Nb, Mo, Ta, and W pillars. The size effects of TCHEAs were relatively small compared with that of conventional alloys [63]. These features could be attributed to solution strengthening and the increased lattice friction due to lattice distortion at atomic length scales [63]. Zou et al. [62] also applied the magnetron sputtering technique to fabricate WNbMoTa thin-film TCHEA with a nanocrystalline structure. The micropillar compression test indicated that TCHEA exhibited an ultrahigh yield strength of 10 GPa. A heat treatment was conducted at 1100 °C for 3 days to illustrate the stability of WNbMoTa TCHEAs with a nanocrystalline structure in Fig. 6. The results showed that WNbMoTa TCHEA could maintain the nanocrystalline structure and exhibit ultrahigh yield strength, which was comparable to the value before the heat treatment. On the contrary, severe grain growth coarsening happened when pure W with the nanocrystalline structure was used for the same heat treatment processing. A large number of studies showed that impurity elements concentrated along the grain boundary and weakened the grain boundary, leading to embrittlement [58]. The coarse-grain alloys showed poor tolerance to impurity elements compared with fine-grained alloys due to the low density of grain boundaries. TCHEAs may be an effective way to suppress recrystallization and brittleness of tungsten-containing materials.

Hence, WNbMoTa TCHEAs were one of the promising model alloys used at elevated temperatures. Many studies

**Fig. 5** **a** Temperature dependence of the yield stress of WNbMoTa and WNbMoTaV. **b** Neutron diffraction patterns of WNbMoTaV. Reproduced with permission from Ref. [17]. Copyright 2011 Elsevier





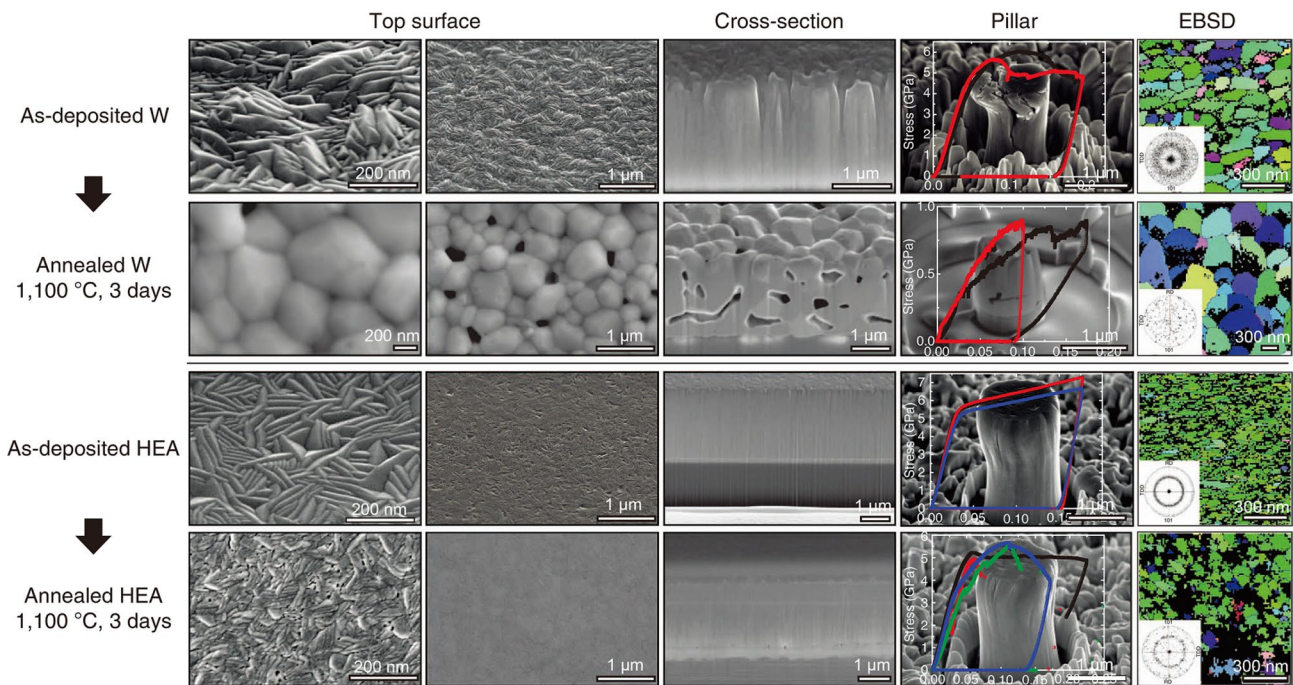


**Fig. 6** Pre- and post-annealing morphology of the W and TCHEA after 3 days at 1100 °C Notes: EBSD, Electron Backscattered Diffraction. Reproduced with permission from Ref. [62] Copyright 2015, Springer Nature

were conducted using Ti [34, 36], Cr [27, 47], and Re [31, 32] addition in WNbMoTa model alloys. Especially, the addition of Ti could significantly increase the plasticity at room temperature and the strength of as-cast WNbMoTa TCHEAs. As shown in Fig. 7, the compressive plasticity increased from 1.9% of WNbMoTa TCHEAs to 11.5% of TiWNbMoTa TCHEAs, and at the same time, the yield strength increased from 996 to 1455 MPa [34].

Long et al. [47] reported a fine-grained CrVWNbMoTa TCHEA consisting of the BCC main phase,  $Ta_2VO_6$  particles, and Laves phase. It established an ultrahigh compressive yield strength of 3416 MPa and acceptable plasticity of 5.3%. Zhang et al. [30] investigated the effect of the addition of Re on WNbMoTa TCHEAs. All as-cast  $Re_xNbMoTaW$  ( $x=0, 0.5$ , and 1) TCHEAs were composed of the BCC

matrix phase and (Nb,Ta)-rich particle precipitation phase.  $Re_{0.5}NbMoTaW$  TCHEAs had the best comprehensive mechanical properties, showing a compressive yield strength of 1147 MPa and plasticity of 7.0%.

## 4.2 Irradiation resistance properties

Low activation property is regarded as an important indicator of structural materials for fusion reactors to ensure that radioactive substances generated by transmutation can be prevented as much as possible [86]. As shown in Fig. 8a [87], materials with low activation meant that radioactive substances had a shorter half-life period and could be safely recycled in less time at the same “hands-on” level. Low-activation steel [88, 89], V–Cr–Ti alloys [90, 91], and

**Fig. 7** **a** Compressive engineering stress-strain curves of WNbMoTaTi<sub>x</sub> **b** yield strength and strain vs. Ti content. Reproduced with permission from Ref. [34]. Copyright 2018 Elsevier

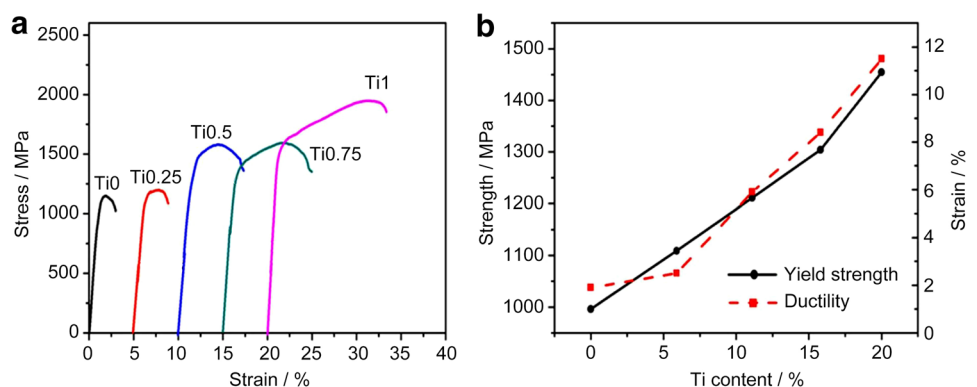
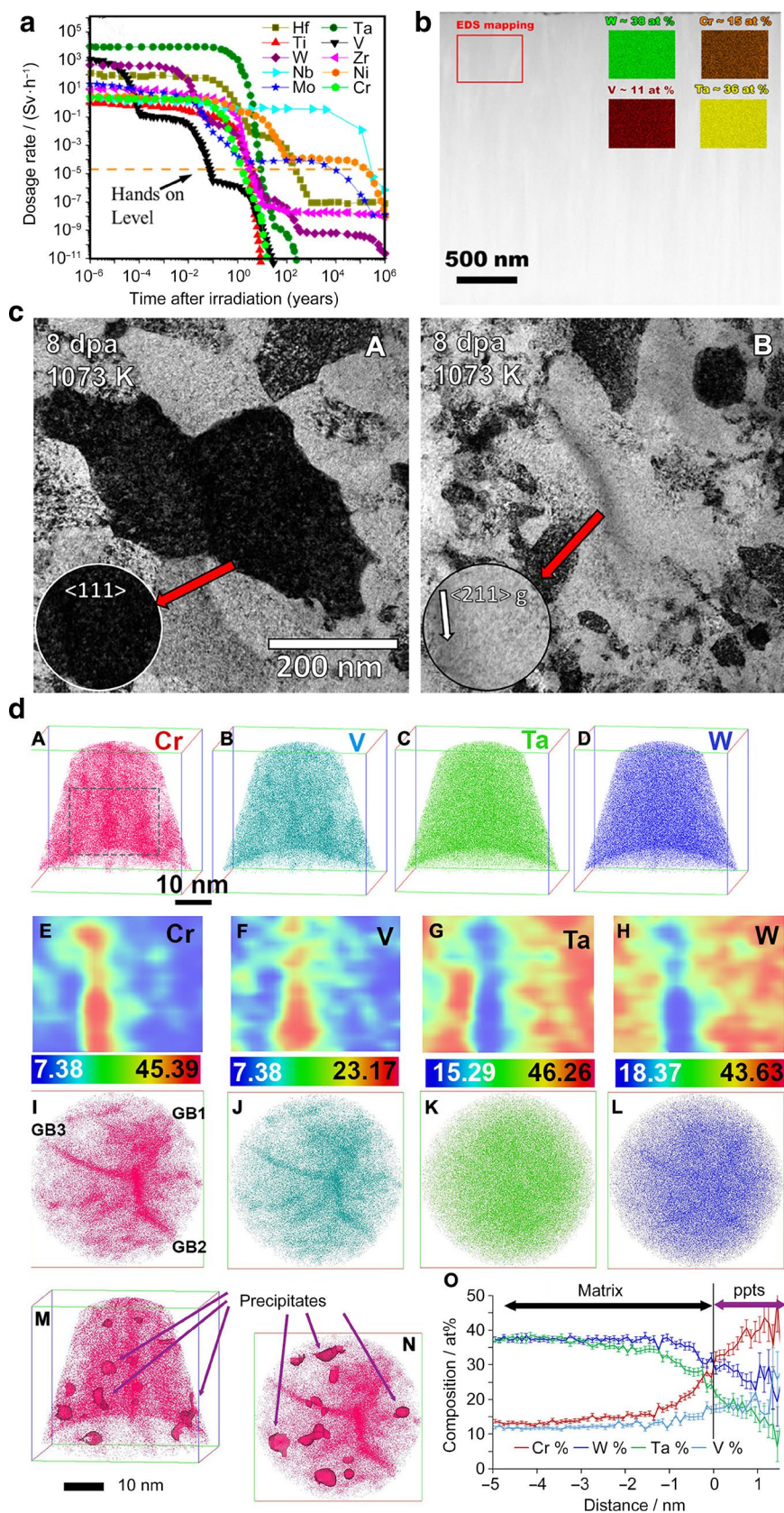


**Fig. 8** Dosage rate versus time in years required for several refractory elements to reach the “hands-on” level after irradiation. Reproduced with permission from Ref. [87]. Copyright 2020, Multidisciplinary Digital Publishing Institute. **b** SEM result of  $W_{38}Ta_{36}Cr_{15}V_{11}$  TCHEA before irradiation. **c** TEM observation of  $W_{38}Ta_{36}Cr_{15}V_{11}$  TCHEA after irradiation under the condition of 8 dpa and 800 °C. **d** Atom probe tomography result of  $W_{38}Ta_{36}Cr_{15}V_{11}$  TCHEA after irradiation. **b–d** Reproduced with permission from Ref. [3]. Copyright 2019, American Association for the Advancement of Science





low-activation HEAs [87, 92] were carefully designed by replacing high-activation elements. For instance, Waseem et al. [1, 2, 59] designed a series of  $W_xTaTiVCr$  TCHEAs consisting of low-activation elements and investigated the influence of W [2] and Ti contents [59] on the mechanical properties and oxidation resistance properties. The results indicated that the hardness and yield strength of  $W_xTaTiVCr$  TCHEAs decreased with the increase in the W content.  $W_{32}(TaTiVCr)_{68}$  TCHEA established high hardness of 768 HV and high compressive yield strength of 2265 MPa, which was superior to that of most W-based binary alloys. The addition of Ti significantly improved the oxidation resistance of  $W_xTaTiVCr$  TCHEAs in the air at 1000 °C. Zhang et al. [23] reported that low-activation  $VCrFeTa_{0.2}W_{0.2}$  TCHEAs had good comprehensive mechanical properties with compressive yield strength of 1742 MPa and compressive plastic strain of 35.7%. Low-activation TCHEAs exhibit high strength, but unfortunately, studies on the irradiation damage behavior and irradiation resistance of TCHEAs are still lacking.

Even so, TCHEAs have enormous potential. El-Atwani et al. [3] studied the irradiation resistance of TCHEAs. They revealed that  $W_{38}Ta_{36}Cr_{15}V_{11}$  TCHEA, consisting of a bimodal grain size distribution (nanocrystalline region of 100 nm and ultrafine grain sizes of 100–500 nm), had outstanding irradiation resistance [3]. As shown in Fig. 8b–d, no irradiation-created dislocation loop was observed by in situ transmission electron microscope (TEM) during the irradiation process even up to 8 dpa (displacement per atom), and only with Cr- and V-rich precipitates appeared along the grain boundary. As a consequence, the change in nanoindentation hardness before and after irradiation was nearly negligible, as obtained by the nanoindentation test. A series of theoretical simulations, including the density functional theory and the cluster expansion methodology, and Monte Carlo simulations were used to reveal the origin of Cr- and V-rich precipitates [3]. The positive mixing enthalpy of  $\Delta H_{mix}$  was regarded as the reason for phase separation [3]. The irradiation resistance mechanism of TCHEAs might be similar to that of Ni-based FCC HEAs [93–95]. The mobilities of vacancies and interstitial atoms were approximate, so that the recombination probability of the defect increased considerably compared with the conventional alloys [19]. The severe lattice distortion in TCHEAs was important in the irradiation process. Severe lattice distortion in TCHEAs made the overlap region between the migration energy of vacancies and interstitials broad [19]. The lattice distortion was also beneficial in delaying the irradiation-induced dislocation loop growth [96]. Severe lattice distortion also changed the morphology of interstitial dumbbells. Interstitial dumbbells of conventional nonmagnetic BCC alloys usually favored the [110]-direction, while that of TCHEAs favored the [111]-direction [19]. In conclusion, the unique mobilities

and formation behavior of defects and the lattice distortion were all regarded as the origin of the outstanding irradiation resistance of TCHEAs.

## 5 Summary and future development

TCHEAs are a special part of the HEA family because of the addition of ultrahigh-melting point element W. The manufacturing routes and phase selection rules of TCHEAs are slightly different from those of other HEAs. Moreover, TCHEAs exhibit excellent high-temperature mechanical properties and unique irradiation resistance properties. In this study, the details of manufacturing routes of TCHEAs were presented and the applicability of several representative empirical parametric models for TCHEAs was reevaluated. Finally, the latest developments in mechanical properties and irradiation resistance properties of TCHEAs were reviewed.

A research needs to be carried out from the following aspects to further develop TCHEAs. First, an advanced model of phase selection should be conducted for TCHEAs, such as machine learning and data mining, due to the limitation and inefficiency of the empirical parametric model. Second, the inferior plasticity of TCHEAs at room temperature should be improved further by adjusting the alloy composition and optimizing the preparation process. Finally, the strengthening and toughening mechanism and irradiation damage mechanism in TCHEAs, which is essential for TCHEAs to be a promising candidate for PFMs.

**Acknowledgements** This work was financially supported by National MCF Energy Research and Development Program (Grant No. 2018YFE0312400), National Natural Science Foundation of China (Grant Nos. 51822402 and 51671044), National Key Research and Development Program of China (Grant Nos. 2019YFA0209901 and 2018YFA0702901), Liao Ning Revitalization Talents Program (Grant No. XLYC1807047), Fund of Science and Technology on Reactor Fuel and Materials Laboratory (Grant No. 6142A06190304), and Fund of the State Key Laboratory of Solidification Processing in Northwestern Polytechnical University (Grant No. SKLSP201902)

## References

1. Waseem OA, Ryu HJ. Toughening of a low-activation tungsten alloy using tungsten short fibers and particles reinforcement for fusion plasma-facing applications. *Nucl Fus.* 2019;59(2):026007.
2. Waseem OA, Ryu HJ. Powder metallurgy processing of a  $W_xTaTiVCr$  high-entropy alloy and its derivative alloys for fusion material applications. *Sci Rep.* 2017;7(1):1926.
3. El-Atwani O, Li N, Li M, Devaraj A, Baldwin JKS, Schneider MM, Sobieraj D, Wróbel JS, Nguyen-Manh D, Maloy SA, Martinez E. Outstanding radiation resistance of tungsten-based high-entropy alloys. *Sci Adv.* 2019;5(3):eaav2002.
4. Wang Q, Du G, Chen N, Jiang C, Chen L. Ideal strengths and thermodynamic properties of W and W-Re alloys from first-principles calculation. *Fus Eng Des.* 2020;155:111579.

5. Li J, Wei Z, Zhou B, Wu Y, Chen SG, Sun Z. Preparation, microstructure, and microhardness of selective laser-melted W–3Ta sample. *J Mater Res*. 2020;35(15):2016.
6. Chen CL, Sutrisna. Influence of alloying elements, in-situ dispersoids and fabrication on microstructure and properties of W-(Ta,V,Ti) ODS alloys. *J Alloys Compd*. 2020;834:154952.
7. Wang ZL, Gao WJ, Liu YL, Li R, Meng FS, Song JP, Qi Y. A first principles investigation of  $W_{1-x}Mo_x$  ( $x = 0-68.75$  at.%) alloys: Structural, electronic, mechanical and thermal properties. *J Alloys Compd*. 2020;829:154480.
8. Yan J, Li X, Wang Z, Zhu K. Comparison of surface morphologies and helium retention of nanocrystalline W and W-Cr films prepared by magnetron sputtering. *Nucl Mater Energy*. 2020;22:100733.
9. Zhang Y, Liu JP, Chen SY, Xie X, Liaw PK, Dahmen KA, Qiao JW, Wang YL. Serration and noise behaviors in materials. *Prog Mater Sci*. 2017;90:358.
10. Cantor B, Chang ITH, Knight P, Vincent AJB. Microstructural development in equiatomic multicomponent alloys. *Mater Sci Eng A*. 2004;375–377:213.
11. George EP, Raabe D, Ritchie RO. High-entropy alloys. *Nat Rev Mater*. 2019;4(8):515.
12. Zhu M, Yao L, Liu Y, Zhang M, Li K, Jian Z. Microstructure evolution and mechanical properties of a novel CrNbTiZrAl<sub>x</sub> ( $0.25 \leq x \leq 1.25$ ) eutectic refractory high-entropy alloy. *Mater Lett*. 2020;272:127869.
13. Zhrebtsov S, Yurchenko N, Shaysultanov D, Tikhonovsky M, Salishchev G, Stepanov N. Microstructure and mechanical properties evolution in HfNbTaTiZr refractory high-entropy alloy during cold rolling. *Adv Eng Mater*. 2020;22(10):2000105.
14. Yurchenko N, Panina E, Tikhonovsky M, Salishchev G, Zhrebtsov S, Stepanov N. Structure and mechanical properties of an in situ refractory Al<sub>20</sub>Cr<sub>10</sub>Nb<sub>15</sub>Ti<sub>20</sub>V<sub>25</sub>Zr<sub>10</sub> high entropy alloy composite. *Mater Lett*. 2020;264:127372.
15. Yang T, Guo W, Poplawsky JD, Li D, Wang L, Li Y, Hu W, Crespi ML, Yan Z, Zhang Y, Wang Y, Zinkle SJ. Structural damage and phase stability of Al<sub>0.5</sub>CoCrFeNi high entropy alloy under high temperature ion irradiation. *Acta Mater*. 2020;188:1.
16. Wang F, Yan X, Wang T, Wu Y, Shao L, Nastasi M, Lu Y, Cui B. Irradiation damage in (Zr<sub>0.25</sub>Ta<sub>0.25</sub>Nb<sub>0.25</sub>Ti<sub>0.25</sub>)C high-entropy carbide ceramics. *Acta Mater*. 2020;195:739.
17. Senkov ON, Wilks GB, Scott JM, Miracle DB. Mechanical properties of Nb<sub>25</sub>Mo<sub>25</sub>Ta<sub>25</sub>W<sub>25</sub> and V<sub>20</sub>Nb<sub>20</sub>Mo<sub>20</sub>Ta<sub>20</sub>W<sub>20</sub> refractory high entropy alloys. *Intermetallics*. 2011;19(5):698.
18. Senkov ON, Wilks GB, Miracle DB, Chuang CP, Liaw PK. Refractory high-entropy alloys. *Intermetallics*. 2010;18(9):1758.
19. Zhao S. Defect properties in a VTaCrW equiatomic high entropy alloy (HEA) with the body centered cubic (bcc) structure. *J Mater Sci Technol*. 2020;44:133.
20. Wang L, Wang L, Tang Y, Luo L, Luo L, Su Y, Guo J, Fu H. Microstructure and mechanical properties of CoCrFeNiW high entropy alloys reinforced by  $\mu$  phase particles. *J Alloy Compd*. 2020;843:155997.
21. Jiang H, Huang TD, Su C, Zhang HB, Han KM, Qin SX. Microstructure and mechanical behavior of CrFeNi<sub>2</sub>V<sub>0.5</sub>W<sub>x</sub> ( $x=0, 0.25$ ) high-entropy alloys. *Acta Metall Sinica (Engl Lett)*. 2020;33(8):1117.
22. Ley NA, Segovia S, Gorsse S, Young ML. Characterization and modeling of NbNiTaTiW and NbNiTaTiW-Al refractory high-entropy alloys. *Metall Mater Trans A*. 2019;50(10):4867.
23. Zhang W, Liaw P, Zhang Y. A novel low-activation VCrFeTa<sub>x</sub>W<sub>x</sub> ( $x = 0.1, 0.2, 0.3, 0.4$ , and 1) high-entropy alloys with excellent heat-softening resistance. *Entropy*. 2018;20(12):951.
24. Jiang H, Zhang H, Huang T, Lu Y, Wang T, Li T. Microstructures and mechanical properties of Co<sub>2</sub>Mo<sub>x</sub>Ni<sub>2</sub>VW<sub>x</sub> eutectic high entropy alloys. *Mater Des*. 2016;109:539.
25. Jiang H, Jiang L, Han K, Lu Y, Wang T, Cao Z, Li T. Effects of tungsten on microstructure and mechanical properties of CrFeNiV<sub>0.5</sub>W<sub>x</sub> and CrFeNi<sub>2</sub>V<sub>0.5</sub>W<sub>x</sub> high-entropy alloys. 2015;24(12):4594.
26. Wang M, Ma Z, Xu Z, Cheng X. Microstructures and mechanical properties of HfNbTaTiZrW and HfNbTaTiZrMoW refractory high-entropy alloys. *J Alloy Compd*. 2019;803:778.
27. Zhang B, Gao MC, Zhang Y, Guo SM. Senary refractory high-entropy alloy CrMoNbTaVW. *Calphad*. 2015;51:193.
28. Raman L, Karthick G, Guruvidyathri K, Fabijanic D, Narayana Murthy SVS, Murty BS, Kottada RS. Influence of processing route on the alloying behavior, microstructural evolution and thermal stability of CrMoNbTiW refractory high-entropy alloy. *J Mater Res*. 2020;35(12):1556.
29. Wei Q, Shen Q, Zhang J, Chen B, Luo G, Zhang L. Microstructure and mechanical property of a novel ReMoTaW high-entropy alloy with high density. *Int J Refract Metal Hard Mater*. 2018;77:8.
30. Zhang J, Hu Y, Wei Q, Xiao Y, Chen P, Luo G, Shen Q. Microstructure and mechanical properties of Re<sub>x</sub>NbMoTaW high-entropy alloys prepared by arc melting using metal powders. *J Alloy Compd*. 2020;827:154301.
31. Yan D, Song K, Sun H, Wu S, Zhao K, Zhang H, Yuan S, Kim JT, Chawake N, Renk O, Hohenwarter A, Wang L, Eckert J. Microstructures, mechanical properties, and corrosion behaviors of refractory high-entropy ReTaWNbMo alloys. *J Mater Eng Perform*. 2020;29(1):399.
32. Raturi A, Aditya CJ, Gurao NP, Biswas K. ICME approach to explore equiatomic and non-equiatomic single phase BCC refractory high entropy alloys. *J Alloy Compd*. 2019;806:587.
33. Ikeuchi D, King DJM, Laws KJ, Knowles AJ, Aughterson RD, Lumpkin GR, Obbard EG. Cr-Mo-V-W: A new refractory and transition metal high-entropy alloy system. *Scripta Mater*. 2019;158:141.
34. Han ZD, Luan HW, Liu X, Chen N, Li XY, Shao Y, Yao K. Microstructures and mechanical properties of Ti<sub>x</sub>NbMoTaW refractory high-entropy alloys. *Mater Sci Eng A*. 2018;712:380.
35. Yao HW, Qiao JW, Gao MC, Hawk JA, Ma SG, Zhou HF, Zhang Y. NbTaV-(Ti, W) refractory high-entropy alloys: Experiments and modeling. *Mater Sci Eng A*. 2016;674:203.
36. Han ZD, Chen N, Zhao SF, Fan LW, Yang GN, Shao Y, Yao K. Effect of Ti additions on mechanical properties of NbMoTaW and VNbMoTaW refractory high entropy alloys. *Intermetallics*. 2017;84:153.
37. Moorehead M, Bertsch K, Niezgoda M, Parkin C, Elbakhshwan M, Sridharan K, Zhang C, Thoma D, Couet A. High-throughput synthesis of Mo-Nb-Ta-W high-entropy alloys via additive manufacturing. *Mater Des*. 2020;187:108358.
38. Guo Y, Liu Q. MoFeCrTiWAlNb refractory high-entropy alloy coating fabricated by rectangular-spot laser cladding. *Intermetallics*. 2018;102:78.
39. Li Q, Zhang H, Li D, Chen Z, Huang S, Lu Z, Yan H. W<sub>x</sub>NbMoTa refractory high-entropy alloys fabricated by laser cladding deposition. *Materials*. 2019;12(3):533.
40. Zhang M, Zhou X, Yu X, Li J. Synthesis and characterization of refractory TiZrNbWMo high-entropy alloy coating by laser cladding. *Surf Coat Technol*. 2017;311:321.
41. Oleszak D, Antolak-Dudka A, Kulik T. High entropy multicomponent WMoNbZrV alloy processed by mechanical alloying. *Mater Lett*. 2018;232:160.
42. Sun X, Cheng X, Cai H, Ma S, Xu Z, Ali T. Microstructure, mechanical and physical properties of FeCoNiAlMnW high-entropy films deposited by magnetron sputtering. *Appl Surf Sci*. 2020;507:145131.
43. Alvi S, Jarzabek DM, Kohan MG, Hedman D, Jenczyk P, Natile MM, Vomiero A, Akhtar M. Synthesis and mechanical

- characterization of a CuMoTaWV high-entropy film by magnetron sputtering. *ACS Appl Mater Interfaces*. 2020;12(18):21070.
44. Yan J, Li M, Li K, Qiu J, Guo Y. Effects of Cr content on microstructure and mechanical properties of WMoNbTiCr high-entropy alloys. *J Mater Eng Perform*. 2020;29(4):2125.
  45. Ganji RS, Rajulapati KV, Rao KBS. Development of a multi-phase AlCuTaWV high-entropy alloy using powder metallurgy route and its mechanical properties. *Trans Indian Inst Met*. 2020;73(3):613.
  46. Ditenberg IA, Smirnov IV, Korchagin MA, Grinyaev KV, Melnikov VV, Pinzhin YP, Gavrilov AI, Esikov MA, Mali VI, Dudina DV. Structure and phase composition of a W-Ta-Mo-Nb-V-Cr-Zr-Ti alloy obtained by ball milling and spark plasma sintering. *Entropy*. 2020;22(2):143.
  47. Long Y, Liang X, Su K, Peng H, Li X. A fine-grained NbMoTaWVCr refractory high-entropy alloy with ultra-high strength: microstructural evolution and mechanical properties. *J Alloy Compd*. 2019;780:607.
  48. Alvi S, Akhtar F. High temperature tribology of CuMoTaWV high entropy alloy. *Wear*. 2019;426–427:412.
  49. Makhmutov T, Razumov N, Kim A, Ozerskoy N, Mazeeva A, Popovich A. Synthesis of CoCrFeNiMnW<sub>0.25</sub> high-entropy alloy powders by mechanical alloying and plasma spheroidization processes for additive manufacturing. *Metals Mater Int*. 2021;27:50.
  50. Xin SW, Zhang M, Yang TT, Zhao YY, Sun BR, Shen TD. Ultra-hard bulk nanocrystalline VNbMoTaW high-entropy alloy. *J Alloy Compd*. 2018;769:597.
  51. Lo KC, Murakami H, Yeh JW, Yeh AC. Oxidation behaviour of a novel refractory high entropy alloy at elevated temperatures. *Intermetallics*. 2020;119:106711.
  52. Senkov ON, Miracle DB, Chaput KJ, Couzinie JP. Development and exploration of refractory high entropy alloys—a review. *J Mater Res*. 2018;33(19):3092.
  53. Lu Y, Gao X, Jiang L, Chen Z, Wang T, Jie J, Kang H, Zhang Y, Guo S, Ruan H, Zhao Y, Cao Z, Li T. Directly cast bulk eutectic and near-eutectic high entropy alloys with balanced strength and ductility in a wide temperature range. *Acta Mater*. 2017;124:143.
  54. Lu Y, Dong Y, Guo S, Jiang L, Kang H, Wang T, Wen B, Wang Z, Jie J, Cao Z, Ruan H, Li T. A promising new class of high-temperature alloys: eutectic high-entropy alloys. *Sci Rep*. 2014;4:6200.
  55. Park M, Schuh CA. Accelerated sintering in phase-separating nanostructured alloys. *Nat Commun*. 2015;6:6858.
  56. Kang B, Lee J, Ryu HJ, Hong SH. Ultra-high strength WNbMoTaV high-entropy alloys with fine grain structure fabricated by powder metallurgical process. *Mater Sci Eng A*. 2018;712:616.
  57. Tong Y, Qi P, Liang X, Chen Y, Hu Y, Hu Z. Different-shaped ultrafine MoNbTaW HEA powders prepared via mechanical alloying. *Materials*. 2018;11(7):1250.
  58. Zhang T, Deng HW, Xie ZM, Liu R, Yang JF, Liu CS, Wang XP, Fang QF, Xiong Y. Recent progresses on designing and manufacturing of bulk refractory alloys with high performances based on controlling interfaces. *J Mater Sci Technol*. 2020;52:29.
  59. Waseem OA, Lee J, Lee HM, Ryu HJ. The effect of Ti on the sintering and mechanical properties of refractory high-entropy alloy Ti<sub>x</sub>W<sub>1-x</sub>TaV<sub>1-x</sub>Cr<sub>x</sub> fabricated via spark plasma sintering for fusion plasma-facing materials. *Mater Chem Phys*. 2018;210:87.
  60. Han J, Su B, Lu J, Meng J, Zhang A, Wu Y. Preparation of MoNbTaW refractory high entropy alloy powders by pressureless spark plasma sintering: crystal structure and phase evolution. *Intermetallics*. 2020;123:106832.
  61. Wang H, Liu Q, Guo Y, Lan H. MoFe<sub>1.5</sub>CrTiWAlNb<sub>x</sub> refractory high-entropy alloy coating fabricated by laser cladding. *Intermetallics*. 2019;115:106613.
  62. Zou Y, Ma H, Spolenak R. Ultrastrong ductile and stable high-entropy alloys at small scales. *Nat Commun*. 2015;6(1):7748.
  63. Zou Y, Maiti S, Steurer W, Spolenak R. Size-dependent plasticity in an Nb<sub>25</sub>Mo<sub>25</sub>Ta<sub>25</sub>W<sub>25</sub> refractory high-entropy alloy. *Acta Mater*. 2014;65:85.
  64. Feng X, Tang G, Sun M, Ma X, Wang L. Chemical state and phase structure of (TaNbTiW)N films prepared by combined magnetron sputtering and PBI. *Appl Surf Sci*. 2013;280:388.
  65. Melia MA, Whetten SR, Puckett R, Jones M, Heiden MJ, Argibay N, Kustas AB. High-throughput additive manufacturing and characterization of refractory high entropy alloys. *Appl Mater Today*. 2020;19:100560.
  66. Zhao S, Zhang Y, Weber WJ. High entropy alloys: irradiation. *Ref Mod Mater Sci Mater Eng*. 2020. <https://doi.org/10.1016/B978-0-12-803581-8.11713-8>.
  67. Nutor RK, Cao QP, Wang XD, Zhang DX, Fang YZ, Zhang Y, Jiang JZ. Phase selection, lattice distortions, and mechanical properties in high-entropy alloys. *Adv Eng Mater*. 2020;22(11):2000466.
  68. Kube SA, Schroers J. Metastability in high entropy alloys. *Scripta Mater*. 2020;186:392.
  69. Li JH, Tsai MH. Theories for predicting simple solid solution high-entropy alloys: classification, accuracy, and important factors impacting accuracy. *Scripta Mater*. 2020;188:80.
  70. Senkov ON, Miracle DB. A new thermodynamic parameter to predict formation of solid solution or intermetallic phases in high entropy alloys. *J Alloy Compd*. 2016;658:603.
  71. Ye YF, Wang Q, Lu J, Liu CT, Yang Y. Design of high entropy alloys: a single-parameter thermodynamic rule. *Scripta Mater*. 2015;104:53.
  72. Wang Z, Huang Y, Yang Y, Wang J, Liu CT. Atomic-size effect and solid solubility of multicomponent alloys. *Scripta Mater*. 2015;94:28.
  73. Troparevsky MC, Morris JR, Kent PRC, Lupini AR, Stocks GM. Criteria for predicting the formation of single-phase high-entropy alloys. *Phys Rev X*. 2015;5(1):11041.
  74. Yang S, Lu J, Xing F, Zhang L, Zhong Y. Revisit the VEC rule in high entropy alloys (HEAs) with high-throughput CALPHAD approach and its applications for material design—A case study with Al-Co-Cr-Fe-Ni system. *Acta Mater*. 2020;192:11.
  75. Yin S, Ding J, Asta M, Ritchie RO. Ab initio modeling of the energy landscape for screw dislocations in body-centered cubic high-entropy alloys. *NPJ Comput Mater*. 2020;6(1):110.
  76. Zhang Y, Wen C, Wang C, Antonov S, Xue D, Bai Y, Su Y. Phase prediction in high entropy alloys with a rational selection of materials descriptors and machine learning models. *Acta Mater*. 2020;185:528.
  77. Singh AK, Kumar N, Dwivedi A, Subramaniam A. A geometrical parameter for the formation of disordered solid solutions in multi-component alloys. *Intermetallics*. 2014;53:112.
  78. Guo S, Hu Q, Ng C, Liu CT. More than entropy in high-entropy alloys: forming solid solutions or amorphous phase. *Intermetallics*. 2013;41:96.
  79. Song H, Tian F, Hu QM, Vitos L, Wang Y, Shen J, Chen N. Local lattice distortion in high-entropy alloys. *Phys Rev Mater*. 2017;1(2):23404.
  80. Lee C, Song G, Gao MC, Feng R, Chen P, Brechtel J, Chen Y, An K, Guo W, Poplawsky JD, Li S, Samaei AT, Chen W, Hu A, Chen W, Hu A, Choo H, Liaw PK. Lattice distortion in a strong and ductile refractory high-entropy alloy. *Acta Mater*. 2018;160:158.
  81. Ye YF, Zhang YH, He QF, Zhuang Y, Wang S, Shi SQ, Hu A, Fan J, Yang Y. Atomic-scale distorted lattice in chemically disordered equimolar complex alloys. *Acta Mater*. 2018;150:182.
  82. Yang X, Zhang Y. Prediction of high-entropy stabilized solid-solution in multi-component alloys. *Mater Chem Phys*. 2012;132(2–3):233.

83. King DJM, Middleburgh SC, McGregor AG, Cortie MB. Predicting the formation and stability of single phase high-entropy alloys. *Acta Mater.* 2016;104:172.
84. Tong Y, Zhao S, Bei H, Egami T, Zhang Y, Zhang F. Severe local lattice distortion in Zr- and/or Hf-containing refractory multi-principal element alloys. *Acta Mater.* 2020;183:172.
85. Ishibashi S, Ikeda Y, Koermann F, Grabowski B, Neugebauer J. Correlation analysis of strongly fluctuating atomic volumes, charges, and stresses in body-centered cubic refractory high-entropy alloys. *Phys Rev Mater.* 2020;4(2):23608.
86. Shimada M, Costley AE, Federici G, Ioki K, Kukushkin AS, Mukhovatov V, Polevoi A, Sugihara M. Overview of goals and performance of ITER and strategy for plasma-wall interaction investigation. *J Nucl Mater.* 2005;337–339:808.
87. Sadeghilaridjani M, Muskeri S, Pole M, Mukherjee S. High-temperature nano-indentation creep of reduced activity high entropy alloys based on 4-5-6 elemental palette. *Entropy.* 2020;22(2):230.
88. Jiang MG, Chen ZW, Tong JD, Liu CY, Xu G, Liao HB, Liao P, Wang XY, Wang M, Xu M, Lao CS. Strong and ductile reduced activation ferritic/martensitic steel additively manufactured by selective laser melting. *Mater Res Lett.* 2019;7(10):426.
89. Qiu G, Zhan D, Li C, Yang Y, Qi M, Jiang Z, Zhang H. Effects of yttrium and heat treatment on the microstructure and mechanical properties of CLAM steel. *J Mater Eng Perform.* 2020;29(1):42.
90. Fan Z, Jóni B, Ribárik G, Ódor É, Fogarassy Z, Ungár T. The Microstructure and strength of a V–5Cr–5Ti alloy processed by high pressure torsion. *Mater Sci Eng A.* 2019;758:139.
91. Ding J, Yang S, Liu G, Li Q, Zhu B, Zhang M, Zhou L, Shang C, Zhan Q, Wan F. Recrystallization nucleation in V-4Cr-4Ti alloy. *J Alloy Compd.* 2019;777:663.
92. Sadeghilaridjani M, Ayyagari A, Muskeri S, Hasannaeimi V, Salloom R, Chen WY, Mukherjee S. Ion irradiation response and mechanical behavior of reduced activity high entropy alloy. *J Nucl Mater.* 2020;529:151955.
93. Zhao S, Osetsky Y, Zhang Y. Preferential diffusion in concentrated solid solution alloys: NiFe NiCo and NiCoCr. *Acta Mater.* 2017;128:391.
94. Wang X, Barr CM, Jin K, Bei H, Hattar K, Weber WJ, Zhang Y, More KL. Defect evolution in Ni and NiCoCr by in situ 2.8 MeV Au irradiation. *J Nucl Mater.* 2019;523:502.
95. Guan H, Huang S, Ding J, Tian F, Xu Q, Zhao J. Chemical environment and magnetic moment effects on point defect formations in CoCrNi-based concentrated solid-solution alloys. *Acta Mater.* 2020;187:122.
96. Tong Y, Velisa G, Zhao S, Guo W, Yang T, Jin K, Lu C, Bei H, Ko JYP, Pagan DC, Zhang Y, Wang L, Zhang FX. Evolution of local lattice distortion under irradiation in medium- and high-entropy alloys. *Materialia.* 2018;2:73.

**Publisher's Note** Springer Nature remains neutral with regard to jurisdictional claims in published maps and institutional affiliations.



**Dr. Yi-Ping Lu** is a professor of Materials Science and Engineering at the Dalian University of Technology (DUT), China. Prof. Lu was selected as the Young and Middle-aged Innovation Leaders of the “Ministry of Science and Technology of China”, the “Outstanding Youth Fund of the National Natural Science Foundation of China”, the Top Youth Talents of Liaoning Province, and the Outstanding Young Scientific and Technological Talents of Dalian City. His research mainly focuses on composition

design, smelting, solidified structure control, microstructural analysis and performance test of high-entropy alloys (HEAs).